Korean J. Chem. Eng., 40(3), 539-547 (2023)
DOI: 10.1007/s11814-022-1364-0

pISSN: 0256-1115
eISSN: 1975-7220

Data-driven designs and multi-scale simulations of enhanced ion transport in low-temperature operation for lithium-ion batteries

Hongjun Chang*,‡, Yoojin Park*,‡, Ju-Hee Kim*, Seowan Park*, Byung Gon Kim,***,†, and Janghyuk Moon*,†**

*School of Energy Systems Engineering, Chung-Ang University, 84 Heukseok-ro, Dongjak-gu, Seoul 06974, Korea
**Next Generation Battery Research Center, Korea Electrotechnology Research Institute (KERI),
12, Jeongiui-gil, Seongsan-gu, Changwon-si, Gyeongsangnam-do 51543, Korea
***Electro-functional Materials Engineering, University of Science and Technology (UST),
217, Gajeong-ro, Yuseong-gu, Daejeon 34113, Korea
(*Received 1 September 2022 • Revised 29 November 2022 • Accepted 4 December 2022*)

Abstract−The low-temperature operation of lithium-ion batteries (LIBs) is a challenge in achieving high-stability battery technology. Moreover, the design and analysis of low-temperature electrolytes are impeded by the limited understanding of various solvent components and their combinations. In this study, we present a data-driven strategy to design electrolytes with high ionic conductivity at low temperature using various machine-learning algorithms, such as random forest and feedforward neural networks. To establish a link between prediction of electrolyte chemistry and cell performance of LIBs, we performed parameter-free molecular dynamics (MD) prediction of various salt concentrations and temperatures for target solvents. Finally, electrochemical modeling was performed using these properties as the required material parameters. Combining works of the fully parameterized Newman models, parameter-free MD, and data-driven prediction of electrolyte chemistry can help measure the discharge voltage of batteries and enable *in silico* engineering of electrolyte development for realizing low-temperature operation of LIBs.

Keywords: Low Temperature, Electrolyte, Machine Learning, Multi-scale Simulation, Molecular Dynamics, Ion-conductivity

INTRODUCTION

Commercially available lithium-ion batteries (LIBs) for energy storage systems and electric vehicles are typically based on organic liquid electrolytes with Li-ion chemistry [1-3]. For the successful operation of LIBs in worst case scenarios, such as in exterior environments in winter or outer space, predicting the transport properties of organic liquid electrolytes is crucial for further development of LIBs with fast charging/discharging and low-temperature operation capabilities [4-6]. However, evaluating transport properties of developed liquid electrolytes is very time consuming, and finding a direct link between the electrolyte chemistry and cell performance is difficult [7]. Furthermore, Li-ion desolvation and transport are generally affected by the solvent environment, which is composed of solvent and salt molecules in various solvated structures with multiple components [8,9]. Because of the complex configurations of solvents, high-throughput screening and data-driven prediction were performed to find new electrolytes and proper solvent compositions with targeted transportation [10-15].

Most conventional solvents used for achieving high transport characteristics of liquid electrolytes are reasonably well understood in terms of properties such as dielectric constant and viscosity [16-20]. Moreover, melting points of solvents play an important role in low-temperature performance of LIBs [21]. Among various liquid organic molecules, ethylene carbonate (EC) is an essential solvent owing to high salt dissociation and stable formation of the solid electrolyte interphase (SEI) on the electrode-electrolyte interface, having a high dielectric constant (~90) [22-24]. However, its melting temperature is 307 K, which is greater than ambient conditions; consequently, EC is in the solid phase under ambient conditions. To take advantage of EC as a solvent and reduce its melting temperature, mixing it with ethyl methyl carbonate (EMC) molecule is considered a solution [25-27]. Although EMC-based solvents with a lower melting point (~220 K) mitigate the melting point issue of EC solvents, using multicomponent EC/EMC solvents leads to low ionic conductivity (<5 mS/cm at 273 K) [27], which results in Li dendrite growth on graphite and Li metal surface during charging and discharging operations [28,29]. Ternary or quaternary solvent mixtures have been tested to enhance Li-ion conductivity at low temperature [9,30,31]. Furthermore, the rational design of electrolytes with multicomponent solvents has been performed by designing experiment approaches [32,33]. However, selection from the enormous variety of solvent compositions as well as difficulty in characterizing cell performance through tests remain challenging [34]. In addition to electrolyte screening, accurate description of the concentration-dependent transport properties through molecular-level simulation is crucial [35].

In this study, we demonstrate data-driven prediction of the transport properties of multicomponent electrolytes under various conditions such as varying temperature and salt concentration. Using an autoencoder, we suggest the input description of multicompo-

†To whom correspondence should be addressed.
E-mail: byunggonkim@keri.re.kr, jhmoon84@cau.ac.kr
‡These authors are equally contributed.
Copyright by The Korean Institute of Chemical Engineers.

nent electrolytes, which are generated from input features of each single solvent. For selecting and predicting multicomponent solvents for low-temperature electrolytes, machine-learning algorithms, such as feedforward neural networks (FNNs) and random forest (RF), were employed [36]. Parameter-free molecular dynamic (MD) simulations were performed to measure ionic conductivity, diffusivity, and transport number of Li ions with various salt concentrations and working temperatures. A fully parameterized Newman electrochemical model can measure discharge cell voltage and enable *in silico* engineering of electrolyte development for low-temperature operation of LIBs.

COMPUTATIONAL DETAILS

1. Deep-learning Method

Datasets for predicting ionic conductivity were prepared from experimental observation [37]. The types of single electrolytes are listed in Table S1, and input features values are plotted in Fig. S1. Among the various input features, binding energies with Li, highest occupied molecular orbital (HOMO), lowest unoccupied molecular orbital (LUMO) values were calculated using density functional theory (DFT) calculation in DMOL3 implemented in BIOVIA Material Studio [38,39]. From various input features, we selected nine features: temperature, composition rate (EC, EMC, etc.), salt concentration, dielectric constant, melting point, boiling point, viscosity, chemical stability window, and Li-ion binding energy. For multicomposition electrolytes, we designed autoencoder and decoder algorithms to reduce the vector size of binary, ternary, and quaternary electrolytes to that of a single electrolyte [40]. Latent variables were considered input features of multicomposition electrolytes for machine learning and deep neural network algorithms. Further, FNN and RF machine-learning algorithms were selected as representative methods to predict the ionic conductivity of multicomponent electrolytes [41-43]. The detailed schematic and process of prediction using data-driven machine learning are shown in Fig. 1.

2. Molecular Dynamics Simulation

For analyzing the movement of salt and solvent in the electrolyte, MD simulations were performed in BIOVIA Material Studio [44]. All calculations were performed using COMPASS force field in energy tab, which is the latest and proper force field to simulating ionic liquid species [45]. The atomic model structure for salt diffusion calculation was set using Amorphose cell calculation modulus, and the density of the model structure was set to 1.2 g/cm^3, which was the experimentally known value [35]. After setting the value, cell calculation was repeated and then an energetically stable structure was selected. For calculating the movement of salt, every constructed cell was calculated using the dynamics task. In the dynamics task, there is a setting area in every tab, which comprises dynamics, thermostat, and barostat. Ensemble was selected in the order of NVT and NPT ensemble; the temperature was set depending on the simulation temperature; and the total simulation time was 5 ns at NVT, 10 ns at NPT, and 12 ns at NPT sequentially [46,47]. Thermostat and barostat tabs were chosen for temperature and pressure control, respectively. The Nosé-Hoover and

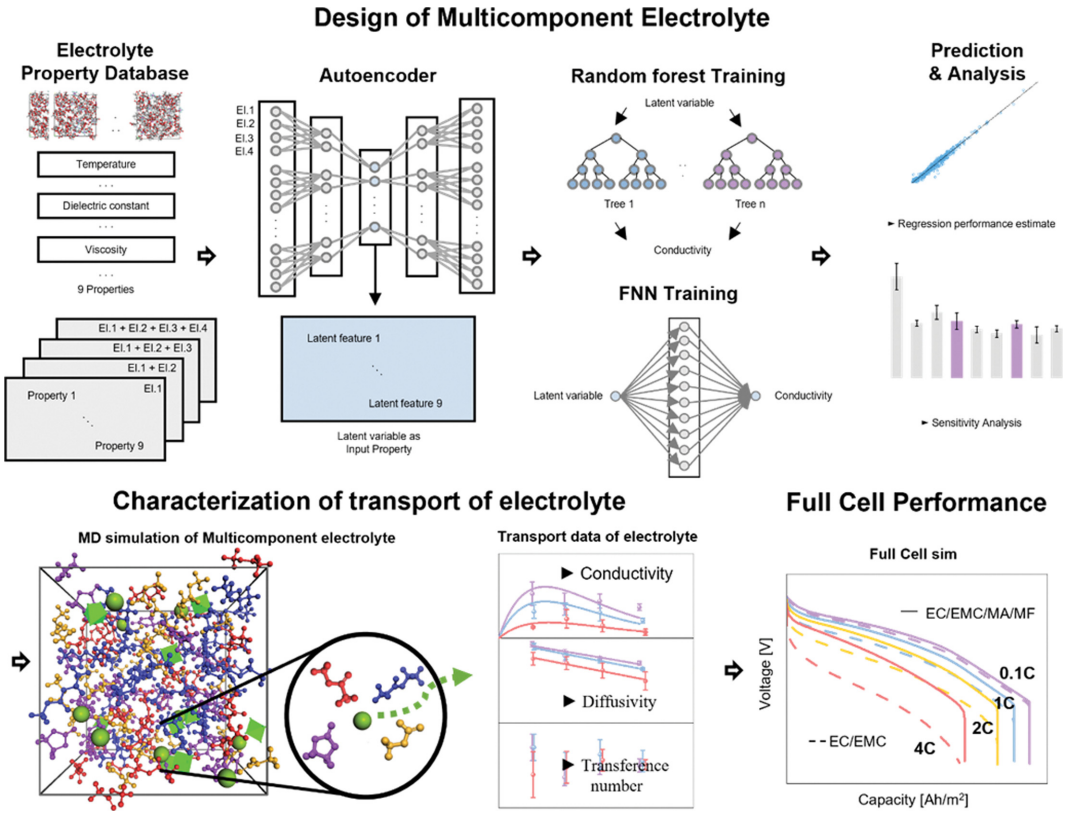


Fig. 1. Schematic of machine learning algorithms to predict transport properties of multicomponent electrolytes and multiscale simulation to characterize transport behaviors and cell performance using molecular dynamics (MD) and battery full-cell simulation.

Berendsen algorithms were used to calculate salt ion-transport properties. After dynamics simulation, mean-square displacement (MSD) analysis was performed from 2.5 to 6.0 ns for Li cation and PF_6 anion. With the values from dynamics simulation, diffusion coefficient, conductivity, and transference number were obtained using Eqs. (1)-(4).

To calculate conductivity and diffusion coefficient, the MD calculation method described in the computational chapter was used. For finding the values related to diffusion, Fick's second law (Eq. (1)) should be considered to analyze a molecule's movement. After solving the three-dimensional Fick's second equation, the relation between diffusion coefficient and MSD can be given by Eq. (2) [48].

$$\frac{\partial C}{\partial t} = D\frac{\partial^2 C}{\partial x^2} \tag{1}$$

$$D = \frac{1}{6N_\alpha t}\lim_{t\to\infty}\frac{d}{dt}\Sigma_{i=1}^{N_\alpha}\langle[r_i(t)-r_0(t)]^2\rangle \tag{2}$$

Because the NVT and NPT ensembles perform calculation according to time, the simulation method can provide the value of the MSD of $LiPF_6$ salt. The following equations and diffusion coefficient of positive and negative ions can also be used to calculate transference number. This value represents the criterion for Li cation migration and a measure of the influence it has on the cell and given condition.

$$t_{Li+} = \frac{D_{Li+}}{D_{Li+}+D_{PF_6-}} \tag{3}$$

The conductivity of salt in the molecular structure can be calculated using a computational method depending on time, volume, and pressure. The Nernst-Einstein equation represents the relation between diffusion coefficient and conductivity:

$$\kappa = \frac{(v_+z_+^2D_- + v_-z_-^2D_+)F^2}{RT} \tag{4}$$

where k is the conductivity, $D_{+/-}$ is the diffusion coefficient, $v_{+/-}$ is the ion concentration (mol/L), $z_{+/-}$ is the valence of anion/cation, F is the Faraday constant, R is the gas constant, and T is the temperature. Conductivity is a measure of how an ion can transfer in a cell that is constructed under specific conditions. In Eq. (4), only two values can be controlled: temperature and ion concentration. MD simulation calculates conductivity and verifies the molecular composite determined using artificial intelligence (AI) has higher conductivity than commercially used electrolytes. From study of properties the AI EC/EMC/MA/MF molecular composite is expected to have high conductivity at low temperatures.

3. Electrochemical Performance

An electrochemical model based on a pseudo two-dimensional (P2D) model was developed to analyze the discharge performance of cells with two different electrolytes (EC/EMC and EC/EMC/MA/MF) at low and room temperatures [49]. The cells were discharged with different C-rates (0.1C, 1C, 2C and 4C).

In each simulation, electrolyte properties, such as ionic conductivity, diffusion coefficient, and transport number values, were obtained from the MD simulation. The electrochemical model solves five main governing equations: mass and charge conservation equations for each electrode and electrolyte region and Butler-Volmer equation to describe charge-transfer kinetics at the electrode-electrolyte interface [50].

The mass conservation equation for the Li ion in the active material follows Fick's second law and can be expressed in spherical coordinates as Eq. (5):

$$\frac{\partial c_s}{\partial t} + \nabla\cdot(-D_s\nabla c_s) = 0 \tag{5}$$

where c_s and D_s denote the lithium concentration and diffusion coefficient of active material particles, respectively. Similarly, the mass conservation equation in the liquid electrolyte region is given by Eq. (6):

$$\frac{\partial c_l}{\partial t} + \nabla\cdot\left(-D_l\nabla c_l + \frac{i_l t_+}{F}\right) = 0 \tag{6}$$

Here, c_l, D_l, i_l, t_+, and F are the electrolyte concentration, diffusion coefficient of Li ions in the electrolyte, current in the electrolyte, transport number of the electrolyte, and the Faraday constant, respectively. Charge conservation for both electrode and electrolyte regions is based on Ohm's law, where i_s and i_l are the current expressions in the electrode and electrolyte region, respectively.

$$\nabla\cdot i_s = \nabla\cdot(-\sigma_s\nabla\emptyset_s) = 0 \tag{7}$$

$$\nabla\cdot i_l = \nabla\cdot\left((-\sigma_l\nabla\emptyset_l) + \frac{2\sigma_l RT}{F}\left(1+\frac{\partial \ln f}{\partial \ln c_l}\right)(1-t_+)\nabla\ln c_l\right) = 0 \tag{8}$$

where σ_s, $\emptyset_s$, σ_l, $\emptyset_l$, R, and T represent the electrical conductivity of an electrode, electric potential, electrolyte ionic conductivity, electrolyte potential, universal gas constant, and temperature, respectively.

Local current density, i, which is due to the charge-transfer reaction at the electrode-electrolyte interface, is expressed as Eq. (9), where i_0, α_a, α_c, η, and E_{eq} denote the exchange current density, charge-transfer coefficients of the anode and cathode, overpotential of the electrolyte-electrode interface, and the equilibrium potential, respectively. We assumed the oxidation-reduction reactions at the interface to be in the equilibrium state and used 0.5 as the value for α_a and α_c.

$$i = i_0\left(\exp\left(\frac{\alpha_a F\eta}{RT}\right) - \exp\left(\frac{-\alpha_c F\eta}{RT}\right)\right) \tag{9}$$

$$\eta = \emptyset_s - \emptyset_l - E_{eq} \tag{10}$$

The parameters used in this model are listed in Fig. S5.

RESULTS AND DISCUSSION

Designing of electrolytes was based on the dielectric constant, viscosity, and melting temperature in Fig. 2 [51]. The dielectric constant has a correlation of dissociation of Li salt ($LiPF_6$) and is also a key factor in conductivity because it can cause the splitting of Li salt into cations (Li^+) and anions (PF_6^-) in the solvent [1,20]. If the dielectric constant of one molecule is higher than that of other molecules, the cations and anions show a larger distance between them, which represents the proportional relation between dielectric con-

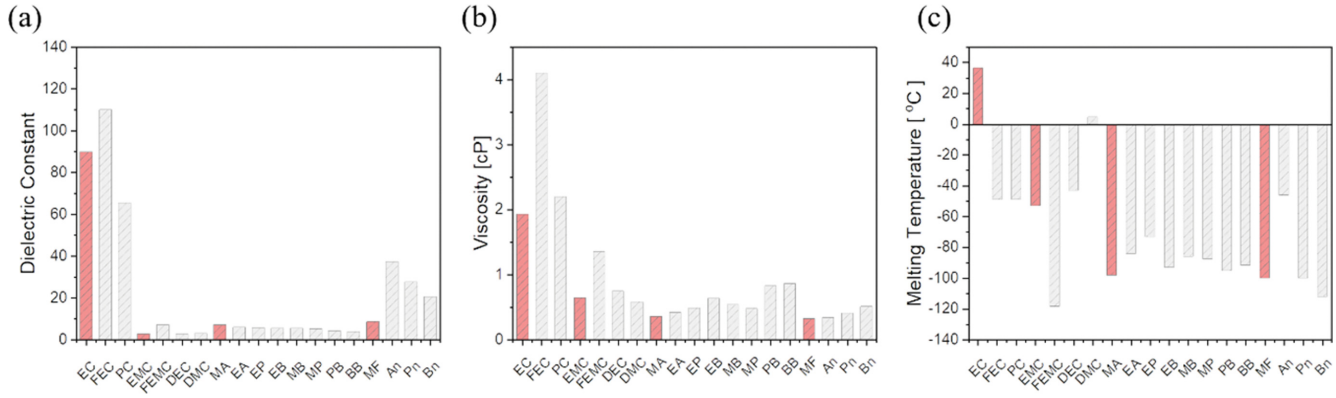


Fig. 2. Intrinsic properties of various electrolyte solvents: (a) dielectric constant, (b) viscosity at room temperature (313 K in EC, FEC) and (c) melting temperature.

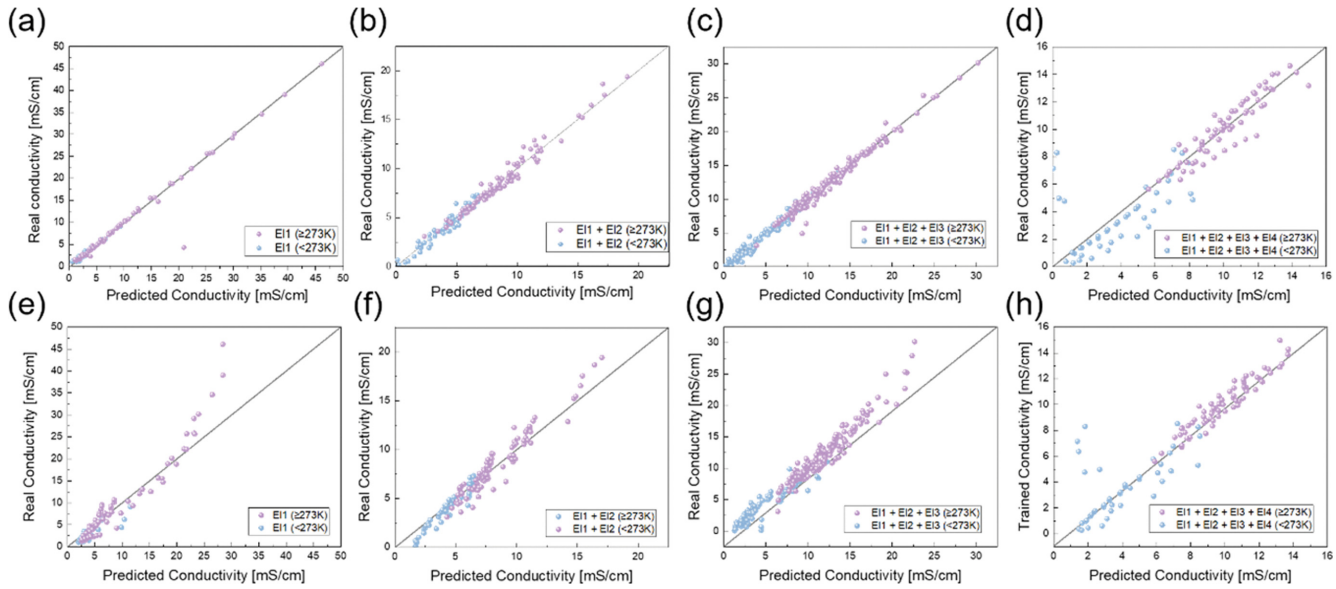


Fig. 3. Prediction results of ionic conductivities of single and multicomponent electrolytes using (a)-(d) FNN and (e)-(h) random forest (RF) algorithm.

stant and high dissociation ability. Among various solvents, EC, FEC, and PC are considered representative solvents owing to their extremely high dielectric values compared with other solvents. In addition, viscosity is a key feature of Li-ion conductivity. From the Stokes-Einstein equation, $D = \frac{k_B T}{C \pi \eta R}$, the ionic conductivity and diffusivity of ion are known to be related to viscosity. Further, melting temperatures of solvents are an essential property for designing low-temperature electrolytes. Because the liquid phase of solvents shows higher transport behavior than the solid phase, the design targets of solvents must sustain liquid states. Although EC has higher dissociation characteristic, it cannot sustain the liquid phase at temperatures below 0 °C. To solve this issue, EC-based multicomponent solvents were designed using various strategies: high dielectric, low viscosity, and low melting point. Because of numerous possible combinations and unpredictable characteristics of synthesized electrolytes, the design of ternary and quaternary solvents for liquid electrolyte is limited.

Figs. 3(a)-(d) show the results of ionic conductivity estimation using the FNN algorithm with single, binary, ternary, and quaternary electrolytes. Because the available datasets are limited, we needed to fully exploit the available dataset. Accordingly, out of 57 different types of electrolytes and 603 different ionic conductivities are trained as temperature as shown in Fig. S1. Overall, FNN provided very accurate ionic conductivity estimation, even in the case of high temperatures (>273 K), while other machine-learning algorithms such as RF in Figs. 3(e)-(f) exhibited high fluctuation. The accuracy of prediction using the FNN and RF algorithms is shown by calculating each root mean square error (RMSE) value in Fig. S4. The binary and ternary electrolytes with 75% sufficient datasets have accuracy, but the single and quaternary electrolytes have bias and deviation due to 35% insufficient datasets. FNN with ten neurons serves as our base structure after hyperparameter tunning of neural networks [52]. FNN showed substantially better performance

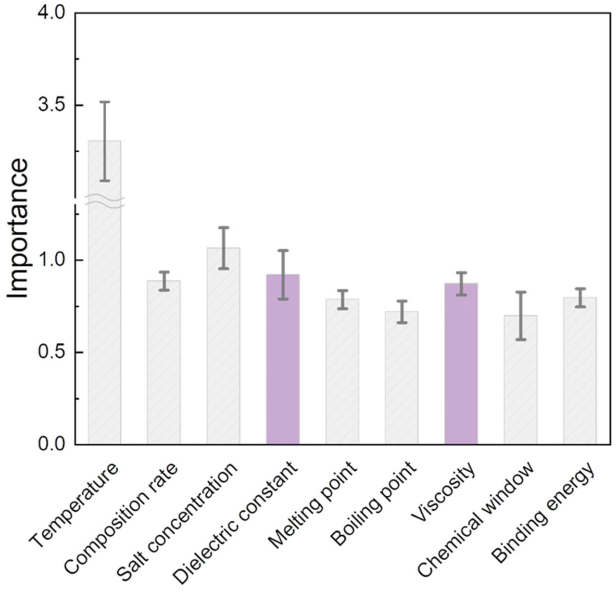


Fig. 4. Sensitivity analysis of electrolyte properties and input variables of RF and FNN studies. The y-axis uses an arbitrary unit.

than other methodologies. This improvement in performance was because latent input vectors from the autoencoder reduced the parameter dimensions of multiple components and the high-dimensional feedforward network regressed more accurately than the RF algorithm.

Although the RF algorithm shows less accurate prediction at room temperature, sensitivity analysis can provide good insight into the design criteria for ionic conductivity from input features. Among the various input features, such as temperature, composition rate (EC, EMC, etc.), salt concentration, dielectric constant, melting point, boiling point, viscosity, chemical stability window, and Li-ion binding energy, which were calculated by DFT calculation, key features are quantified in Fig. 4. Although temperature is the most dominant feature for ionic conductivity, it is a controllable feature for LIB operation. In a similar manner, salt concentration and composition are also design variables for multicomponent electrolytes. We can conclude that dielectric constant and viscosity are the main features in the design of multicomponent electrolytes, which agrees with experimental observations and our discussion.

After implementing the training dataset, the values of ionic conductivity of various compositions of solvent at room and subzero temperatures can be predicted (263 K). Fig. 5 shows the predicted values of ionic conductivity at 263 K with various solvent compositions. The values of ionic conductivity at room temperature are also listed in Fig. S2. Among various solvents, ternary EC/DMC, EC/EMC, and EC/DMC compositions with MA, MF, Bn, and Pn showed higher conductivity values than binary electrolytes. We can infer that the MA, MF, Bn, and Pn additives enhance ionic conductivity in low-temperature operation, although Bn and Pn additives show few such data values. The sample target for quaternary electrolytes was selected using high-throughput screening based on our trained algorithm. EC/EMC/MA/MF showed a conductivity of >8 mS/cm at 263 K. Although Bn- and Pn-added case also showed higher values than others, owing to the data limit, we selected the EC/EMC/MA/MF quaternary electrolyte for the low-temperature LIB electrolyte.

To characterize the EC/EMC electrolyte using MD simulation, dynamic simulations of an EC/EMC molecular cell with 1-M $LiPF_6$ salt were performed five times for each temperature. The diffusion coefficients were derived from the MSD of binary electrolytes, and the mean values were connected to two different linear interpolation lines. The matched points with two interpolation lines were determined as phase-transition points; this solidus line is considered a criterion for changing states of material phases [53]. Although the solid status of the EC solvent is expected below 280 K, the EC/EMC binary electrolyte shows a lower solidus line at 231 K, which is slightly higher than the experimental value of 227 K shown in

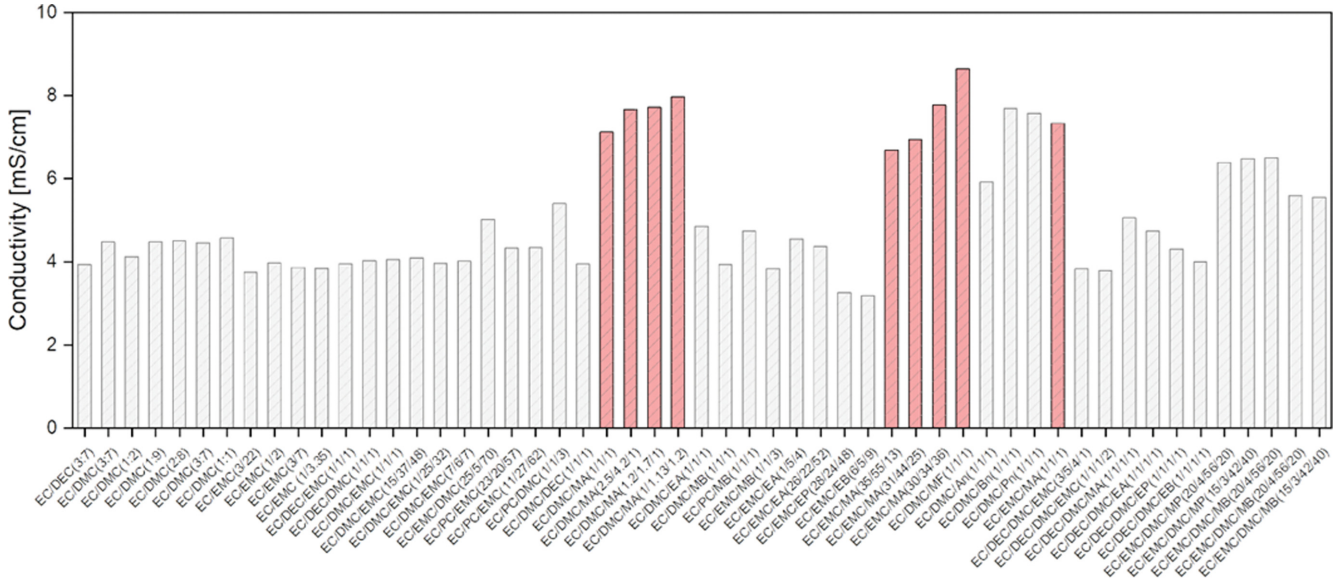


Fig. 5. Predicted ion conductivity of various multicomponent electrolytes using machine-learning algorithms.

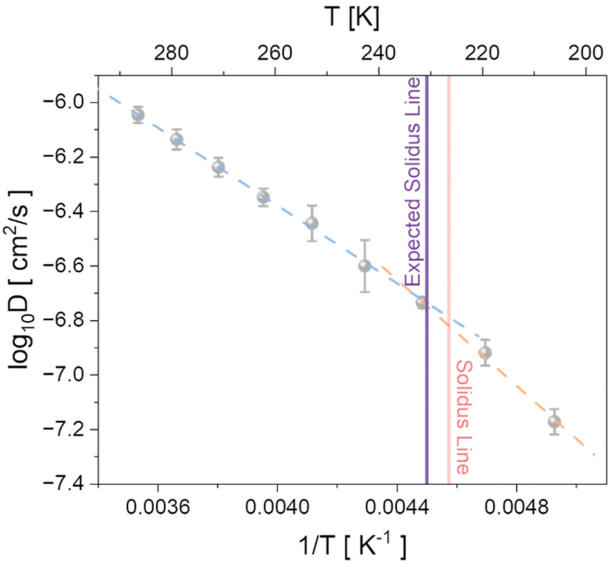


Fig. 6. Solidus line and expected solidus line of EC/EMC solvent calculated using MD simulation with the computational method. The temperatures of the solidus line and expected solidus line are 218.75 and 221.73 K.

Fig. 6. Thus, our MD simulations are well matched with experiments and are expected to characterize transport of Li-ion in multicomponent electrolytes.

Conductivity of the quaternary EC/EMC/MA/MF electrolyte, which was selected from ML studies, was calculated at every 20 K from 293 to 233 K with 1-M $LiPF_6$ salts and 24.7-Å cell length in Fig. 7. The EC/EMC electrolyte, which is commercially popular, showed the lowest conductivity in the temperature range. Further, the electrolytes of EC/EMC/MA and EC/EMC/MF were calculated as a comparative group. At room temperature, MA and MF containing EC/EMC electrolytes exhibited conductivity >10 mS/cm, which was higher than that of EC/EMC (6 mS/cm). Although EC/EMC/MA and EC/EMC/MF showed higher ionic conductivity than EC/EMC and agreed with the ML prediction in Fig. 5, ternary electrolytes of EC/EMC/MA and EC/EMC/MF showed a steep descent decrease with decreasing temperature. However, the quaternary electrolyte of EC/EMC/MA/MF showed linear descent in the subzero temperature range, with four times higher conductivity (6.8 mS/cm) compared with the binary EC/EMC electrolyte (1.8 mS/cm) at 273 K.

For validating the performance of the electrolytes at low temperatures, parameter-free MD simulations were performed to obtain the Li-ion salt concentration-dependent conductivity, diffusion coefficient, and transfer number of Li-ion. Fig. 8(a) shows the dynamics simulation of the EC/EMC binary electrolyte at 263, 298, and 333 K. Our MD dynamic simulations agreed well with previous work [35]. The EC/EMC/MA/MF shown in Fig. 8(b) was also computationally calculated at 253, 273, and 293 K in the low temperature range using the same procedure as that for EC/EMC electrolytes shown in Fig. 8(a). Compared with the experiment observation [54,55], the transfer number of EC/EMC was overestimated by ~0.37-0.4 in the MD simulation. This overestimation resulted from the higher diffusivity of Li-ion in an atomic solvent environment than that in experiments. However, the variation of Li-ion conductivity followed similar trends of experimental observation with respect to salt concentration, which showed peak values of 0.5-1.0 M.

The diffusion coefficient of EC/EMC/MA/MF showed higher values compared with that of EC/EMC in the entire temperatures and smaller change under variation of Li-ion concentration. This result indicates that the quaternary EC/EMC/MA/MF electrolyte needs a small $LiPF_6$ salt concentration, implying that cost-effective salt designing could be achieved.

In the same manner, the conductivity of Li-ion in EC/EMC/MA/MF was also compared with EC/EMC. The EC/EMC/MA/MF had a higher conductivity value of 6.89 mS/cm for a salt concentration of 1.0 M at 253 K; however, EC/EMC showed the highest value

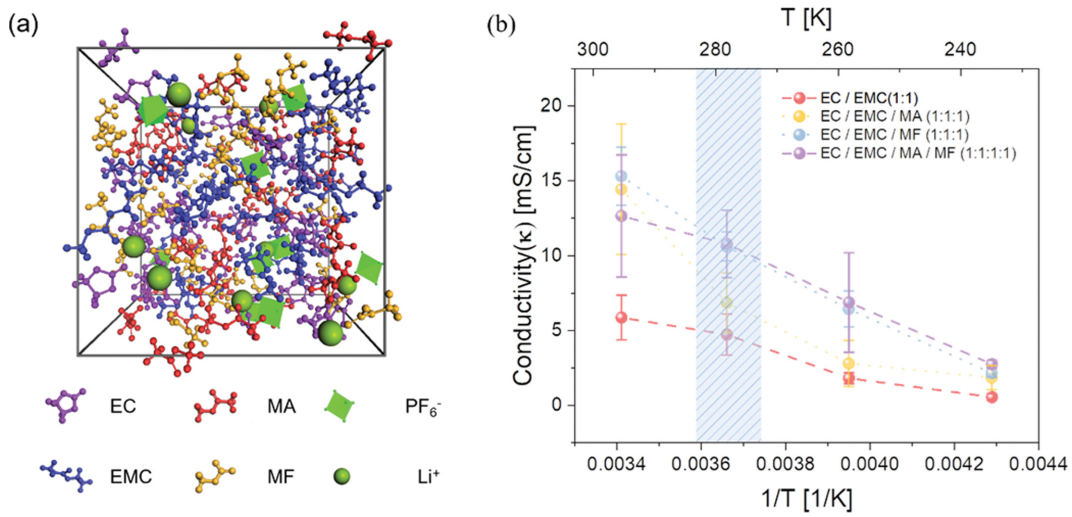


Fig. 7. (a) EC/EMC/MA/MF+$LiPF_6$ cell and conductivity results using MD simulation. (b) A comparison of the conductivity results of four different electrolytes composites with 1-M $LiPF_6$ revealed that the conductivity of EC/EMC/MA/MF was the highest at a low temperature (~233 K).

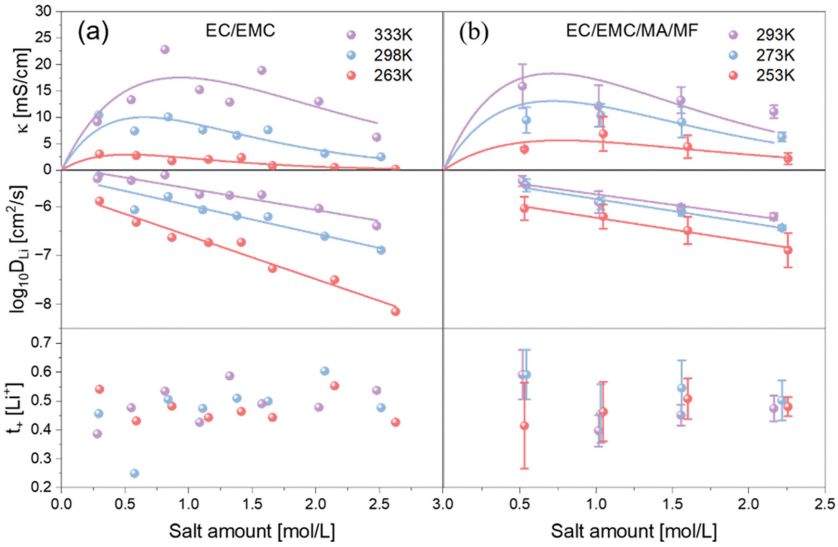


Fig. 8. Conductivity results using MD simulation. A comparison of the conductivity results of (a) EC/EMC and (b) EC/EMC/MA/MF composites with different salt amounts in the electrolyte cell×M $LiPF_6$ (x=0.5/1/1.5/2) revealed that EC/EMC/MA/MF had a higher conductivity value compared with EC/EMC for each salt amount and low temperature (~253 K).

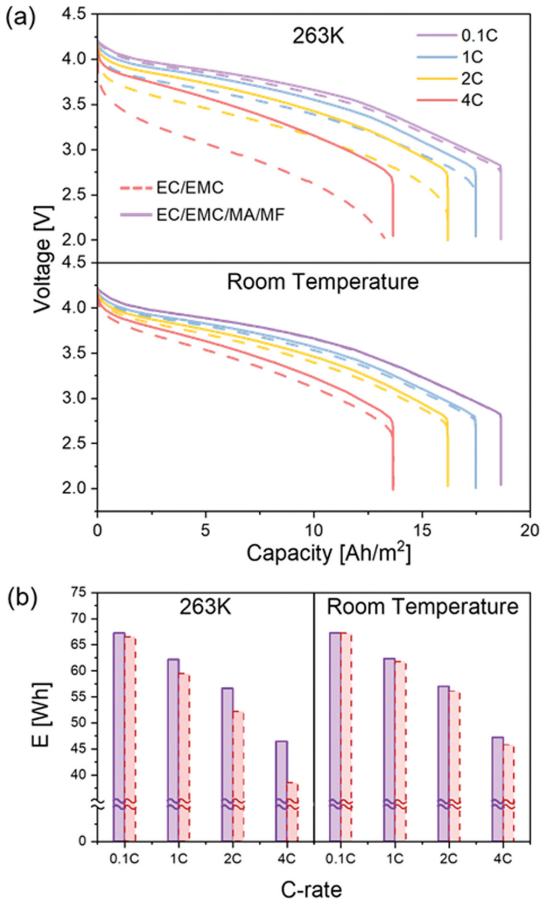


Fig. 9. (a) Discharge profile using LMO ($LiMn_2O_4$)||LiC_6 and selected electrolyte cell; solid lines and dash lines represent EC/EMC/MA/MF and EC/EMC electrolytes, respectively. Selected cells were simulated at two different temperatures and four different C-rates. (b) Energy of two different cells simulated at low temperature and room temperature.

of 2.03 mS/cm at 263 K, which is a higher temperature by 10 K. This tendency was constant for all simulated temperatures and salt amounts. Thus, intrinsic properties of EC/EMC/MA/MF for realizing full-cell characteristics were obtained by parametric-free MD simulation. To scale up the characteristics of low-temperature performance, Newman's electrochemical model was used and compared with the EC/EMC binary electrolyte.

Fig. 9(a) shows the results for discharge rates and different temperatures of binary and quaternary electrolytes with $LiMn_2O_4$ (spinel) and graphite electrodes, covering typical operating conditions in an automotive environment. Fig. 9(b) shows the calculated cell energy of EC/EMC/MA/MF and EC/EMC electrolytes cell at subzero and room temperature. Up to discharge rates of 4C, fast discharge leads to a substantial dissipation of energy, and operation down to a temperature of 263 K also decreases the cell performance owing to low ionic transport of liquid electrolyte inside the battery. Although this study only demonstrated electrolyte transports in low-temperature operation, the EC/EMC/MA/MF electrolyte showed smaller voltage polarization during fast discharging. At room temperature, both binary and quaternary electrolytes showed a smaller gap in all operation conditions within 2% in energy density. This agrees well with experiment results in Fig. S6(b). The enhanced ion-transport characteristics using multicomponent designing can reduce the electrochemical polarization and cell performance in the low-temperature range. The NCM/Graphite full cell with the EC/EMC/MA/MF electrolyte also shows an enhanced energy capacity than that with the EC/EMC electrolyte at 263 K in Fig. S6(a).

CONCLUSIONS

We performed *in silico*-based simulation to design multicomponent electrolytes and determine the link between the molecular characteristics and electrochemical performance. Our *in silico* framework is fully automated for the designed electrolyte composition,

salt concentration, and operating temperature. It creates a path toward the computational exploration of the electrolyte for electrochemical cell performance from chemical space. It can reduce the electrolyte optimization task, which is generally performed at a late stage in the battery cell manufacturing process. Furthermore, designing of the electrolyte formulation using machine learning-based analysis can be implemented on engineering time scales. It can reduce the time required to discover and select novel materials. Moreover, if the research implements more experimental data of electrolytes, multidimensional prediction can be trained with the multichannel input method using the autoencoder algorithm. Finally, we highlight the effect of temperature on electrochemical cell performance using the Newman electrochemical model, which recognizes the electrochemical performance at the cell-level scale. Although a simple setup was used to obtain the temperature dependence qualitatively, our integrated approach of describing the battery operation conduction and characterization of electrolyte chemistry from data-drive insights enables *in silico* engineering of electrolyte development for realizing low-temperature operation of LIBs.

ACKNOWLEDGEMENTS

This research was supported by the Technology Development Program to Solve Climate Changes through the National Research Foundation of Korea (NRF) funded by the Ministry of Science, ICT (NRF-2021M1A2A2038142). This research was also supported by the Chung-Ang University Research Scholarship Grants in 2021.

SUPPORTING INFORMATION

Additional information as noted in the text. This information is available via the Internet at http://www.springer.com/chemistry/journal/11814.

REFERENCES

1. D. Hubble, D. E. Brown, Y. Z. Zhao, C. Fang, J. Lau, B. D. McCloskey and G. Liu, *Energy Environ. Sci.*, **15**, 550 (2022).
2. B. Dunn, H. Kamath and J. M. Tarascon, *Science*, **334**, 928 (2011).
3. S. Dajnowicz, G. Agarwal, J. M. Stevenson, L. D. Jacobson, F. Ramezanghorbani, K. Leswing, R. A. Friesner, M. D. Halls and R. Abel, *J. Phys. Chem. B*, **126**, 6271 (2022).
4. Y. G. Cho, M. Q. Li, J. Holoubek, W. K. Li, Y. J. Yin, Y. S. Meng and Z. Chen, *Acs Energy Lett.*, **6**, 2016 (2021).
5. T. Baba, S. Kajita, T. Shiga and N. Ohba, *Sci. Rep.*, **12**, 7291 (2022).
6. Y. L. Lin, S. Huang, L. Zhong, S. J. Wang, D. M. Han, S. Ren, M. Xiao and Y. Z. Meng, *Energy Storage Mater.*, **34**, 128 (2021).
7. S. J. Tan, W. P. Wang, Y. F. Tian, S. Xin and Y. G. Guo, *Adv. Funct. Mater.*, **31**, 2105253 (2021).
8. X. Tang, D. Xiao, Z. Xu, Q. Liu, B. Ding, H. Dou and X. Zhang, *J. Mater. Chem. A*, **10**, 18374 (2022).
9. Q. Y. Li, S. H. Jiao, L. L. Luo, M. S. Ding, J. M. Zheng, S. S. Cartmell, C. M. Wang, K. Xu, J. G. Zhang and W. Xu, *Acs Appl. Mater. Inter.*, **9**, 18826 (2017).
10. N. Yao, X. Chen, Z. H. Fu and Q. Zhang, *Chem. Rev.*, **122**, 10970 (2022).
11. S. Matsuda, K. Nishioka and S. Nakanishi, *Sci. Rep.*, **9**, 6211 (2019).
12. A. Benayad, D. Diddens, A. Heuer, A. N. Krishnamoorthy, M. Maiti, F. Le Cras, M. Legallais, F. Rahmanian, Y. Shin, H. Stein, M. Winter, C. Wolke, P. Yan and I. Cekic-Laskovic, *Adv. Energy Mater.*, **12**, 2102678 (2022).
13. J. Rodriguez, M. Politi, S. Adler, D. Beck and L. Pozzo, *Mol. Syst. Des. Eng.*, **7**, 933 (2022).
14. J. P. Correa-Baena, K. Hippalgaonkar, J. van Duren, S. Jaffer, V. R. Chandrasekhar, V. Stevanovic, C. Wadia, S. Guha and T. Buonassisi, *Joule*, **2**, 1410 (2018).
15. D. P. Tabor, L. M. Roch, S. K. Saikin, C. Kreisbeck, D. Sheberla, J. H. Montoya, S. Dwaraknath, M. Aykol, C. Ortiz, H. Tribukait, C. Amador-Bedolla, C. J. Brabec, B. Maruyama, K. A. Persson and A. Aspuru-Guzik, *Nat. Rev. Mater.*, **3**, 5 (2018).
16. O. Nordness and J. F. Brennecke, *Chem. Rev.*, **120**, 12873 (2020).
17. J. G. McDaniel and C. Y. Son, *J. Phys. Chem. B*, **122**, 7154 (2018).
18. Q. Y. Dou, S. L. Lei, D. W. Wang, Q. N. Zhang, D. W. Xiao, H. W. Guo, A. P. Wang, H. Yang, Y. L. Li, S. Q. Shi and X. B. Yan, *Energy Environ. Sci.*, **11**, 3212 (2018).
19. T. T. N. Nguyen and M. S. Lee, *J. Mol. Liq.*, **289**, 111112 (2019).
20. A. J. Ringsby, K. D. Fong, J. Self, H. K. Bergstrom, B. D. McCloskey and K. A. Persson, *J. Electrochem. Soc.*, **168**, 080501 (2021).
21. W. X. Lv, C. J. Zhu, J. Chen, C. X. Ou, Q. Zhang and S. W. Zhong, *Chem. Eng. J.*, **418**, 129400 (2021).
22. S. Park, S. Y. Jeong, T. K. Lee, M. W. Park, H. Y. Lim, J. Sung, J. Cho, S. K. Kwak, S. Y. Hong and N. S. Choi, *Nat. Commun.*, **12**, 838 (2021).
23. K. Kim, H. Ma, S. Park and N. S. Choi, *Acs Energy Lett.*, **5**, 1537 (2020).
24. Q. Li, Z. Cao, W. Wahyudi, G. Liu, G. T. Park, L. Cavallo, T. D. Anthopoulos, L. M. Wang, Y. K. Sun, H. N. Alshareef and J. Ming, *Acs Energy Lett.*, **6**, 69 (2021).
25. D. S. Hall, J. Self and J. R. Dahn, *J. Phys. Chem. C*, **119**, 22322 (2015).
26. T. Ohsaki, T. Kishi, T. Kuboki, N. Takami, N. Shimura, Y. Sato, M. Sekino and A. Satoh, *J. Power Sources*, **146**, 97 (2005).
27. M. S. Ding, K. Xu, S. S. Zhang, K. Amine, G. L. Henriksen and T. R. Jow, *J. Electrochem. Soc.*, **148**, A1196 (2001).
28. A. Fly, I. Kirkpatrick and R. Chen, *Appl. Therm. Eng.*, **189**, 116750 (2021).
29. T. T. Vu, G. H. Eom, J. Lee, M. S. Park and J. Moon, *J. Power Sources*, **496**, 229791 (2021).
30. M. C. Smart, B. V. Ratnakumar, L. D. Whitcanack, K. B. Chin, S. Surampudi, H. Croft, D. Tice and R. Staniewicz, *J. Power Sources*, **119**, 349 (2003).
31. M. C. Smart, B. V. Ratnakumar, K. B. Chin and L. D. Whitcanack, *J. Electrochem. Soc.*, **157**, A1361 (2010).
32. M. Giesecke, G. Meriguet, F. Hallberg, Y. Fang, P. Stilbs and I. Furo, *Phys. Chem. Chem. Phys.*, **17**, 3402 (2015).
33. H. Y. Lu, J. S. Hu, L. T. Wang, J. Z. Li, X. Ma, Z. C. Zhu, H. Q. Li, Y. J. Zhao, Y. J. Li, J. X. Zhao and B. G. Xu, *Adv. Funct. Mater.*, **32**, 2112540 (2022).
34. W. R. Xue, T. Qin, Q. Li, M. W. Zan, X. Q. Yu and H. Li, *Energy Storage Mater.*, **50**, 598 (2022).
35. F. Hanke, N. Modrow, R. L. C. Akkermans, I. Korotkin, F. C. Mocanu, V. A. Neufeld and M. Veit, *J. Electrochem. Soc.*, **167**, 013522 (2019).

36. M. Fasahat and M. Manthouri, *J. Power Sources*, **469**, 228375 (2020).
37. N. Zhang, T. Deng, S. Q. Zhang, C. H. Wang, L. X. Chen, C. S. Wang and X. L. Fan, *Adv. Mater.*, **34**, 2107899 (2022).
38. K. Kim, D. Hwang, S. Kim, S. O. Park, H. Cha, Y. S. Lee, J. Cho, S. K. Kwak and N. S. Choi, *Adv. Energy Mater.*, **10**, 2070069 (2020).
39. S. A. Han, H. Qutaish, M. S. Park, J. Moon and J. H. Kim, *Chem-Asian J.*, **16**, 4010 (2021).
40. Z. Y. Xu, Y. J. Guo and J. H. Saleh, *Neural Comput. Appl.*, **34**, 15997 (2022).
41. K. L. Liu, X. S. Hu, H. Y. Zhou, L. Tong, W. D. Widanage and J. Marco, *Ieee-Asme T Mech.*, **26**, 2944 (2021).
42. Y. Li, C. F. Zou, M. Berecibar, E. Nanini-Maury, J. C. W. Chan, P. van den Bossche, J. Van Mierlo and N. Omar, *Appl. Energy*, **232**, 197 (2018).
43. Y. Choi, S. Ryu, K. Park and H. Kim, *Ieee Access*, **7**, 75143 (2019).
44. R. L. C. Akkermans, N. A. Spenley and S. H. Robertson, *Mol. Simulat.*, **39**, 1153 (2013).
45. R. L. C. Akkermans, N. A. Spenley and S. H. Robertson, *Mol. Simulat.*, **47**, 540 (2021).
46. S. Lee, J. Moon, H. M. Bintang, S. Shin, H. G. Jung, S. H. Yu, S. H. Oh, D. Whang and H. D. Lim, *J. Mater. Chem. A*, **9**, 10838 (2021).
47. A. Khetan, H. R. Arjmandi, V. Pande, H. Pitsch and V. Viswanathan, *J. Phys. Chem. C*, **122**, 8094 (2018).
48. J. Moon, B. Lee, M. Cho and K. Cho, *J. Power Sources*, **328**, 558 (2016).
49. D. W. Kang, S. S. Park, H. J. Choi, J. H. Park, J. H. Lee, S. M. Lee, J. H. Choi, J. Moon and B. G. Kim, *Acs Nano*, **16**, 11892 (2022).
50. K. H. Park, D. W. Kang, J. W. Park, J. H. Choi, S. J. Hong, S. H. Song, S. M. Lee, J. Moon and B. G. Kim, *J. Mater. Chem. A*, **9**, 1822 (2021).
51. T. T. Feng, G. Z. Yang, S. Zhang, Z. Q. Xu, H. P. Zhou and M. Q. Wu, *Chem. Eng. J.*, **433**, 134138 (2022).
52. K. Sodeyama, Y. Igarashi, T. Nakayama, Y. Tateyama and M. Okada, *Phys. Chem. Chem. Phys.*, **20**, 22585 (2018).
53. S. Shahruddin, G. Jimenez-Serratos, G. J. P. Britovsek, O. K. Matar and E. A. Muller, *Sci. Rep.-Uk*, **9**, 1002 (2019).
54. C. Capiglia, Y. Saito, H. Kageyama, P. Mustarelli, T. Iwamoto, T. Tabuchi and H. Tukamoto, *J. Power Sources*, **81**, 859 (1999).
55. A. Nyman, M. Behm and G. Lindbergh, *Electrochim. Acta*, **53**, 6356 (2008).

Supporting Information

Data-driven designs and multi-scale simulations of enhanced ion transport in low-temperature operation for lithium-ion batteries

Hongjun Chang[*,‡], Yoojin Park[*,‡], Ju-Hee Kim[*], Seowan Park[*], Byung Gon Kim[,***,†], and Janghyuk Moon[*,†]**

*School of Energy Systems Engineering, Chung-Ang University, 84 Heukseok-ro, Dongjak-gu, Seoul 06974, Korea
**Next Generation Battery Research Center, Korea Electrotechnology Research Institute (KERI),
12, Jeongiui-gil, Seongsan-gu, Changwon-si, Gyeongsangnam-do 51543, Korea
***Electro-functional Materials Engineering, University of Science and Technology (UST),
217, Gajeong-ro, Yuseong-gu, Daejeon 34113, Korea
(*Received 1 September 2022 • Revised 29 November 2022 • Accepted 4 December 2022*)

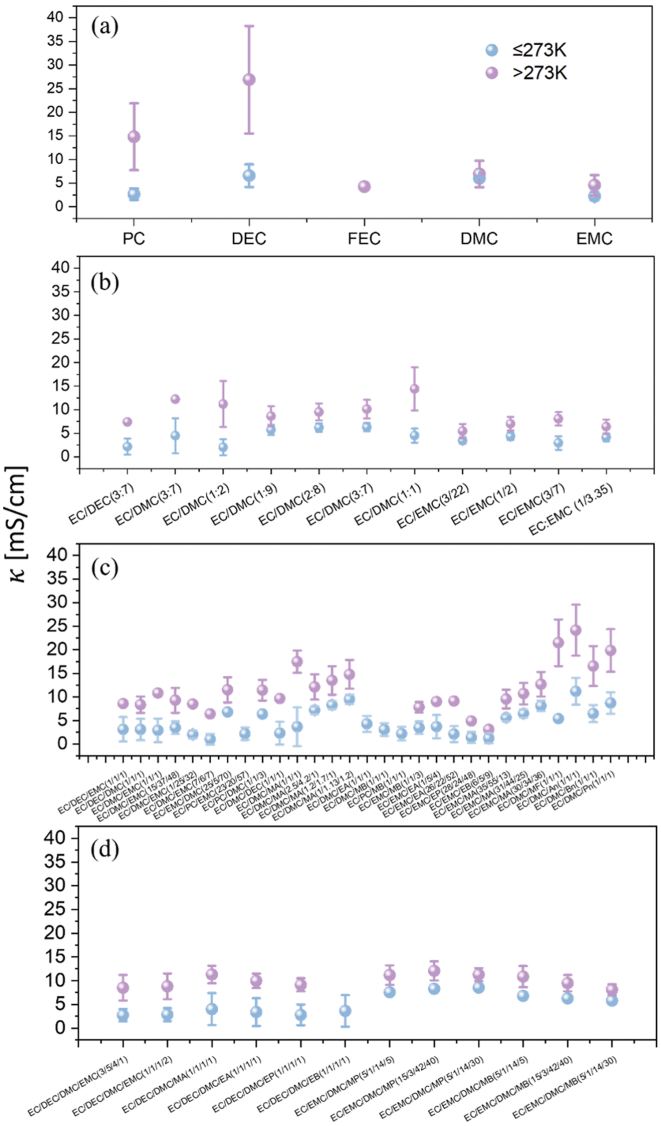


Fig. S1. Training data set to prediction ionic conductivities of multi components electrolytes using various machine learning algorithm: (a) single molecule electrolyte data, (b) double molecules electrolyte data, (c) ternary molecules electrolyte data, (d) quaternary molecules electrolyte data.

Table S1. Information about molecules used in AI Deep learning and MD simulation

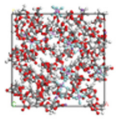
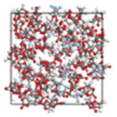
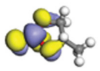
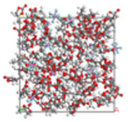
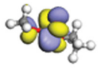
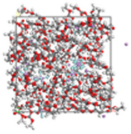
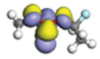
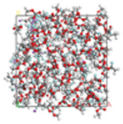
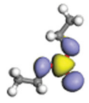
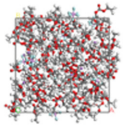
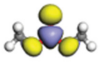
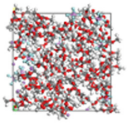
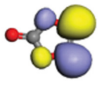
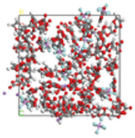
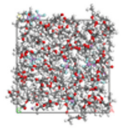
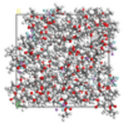
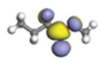
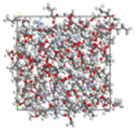
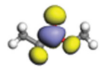
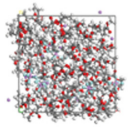
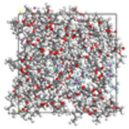
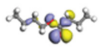
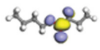
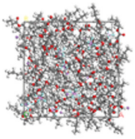
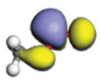
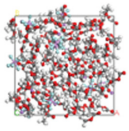
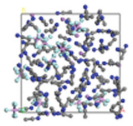
	Molecular Formula	Structural Formular	Li^+ molecule	HOMO	LUMO	Cell construction
EC (Ethylene carbonate)	$C_3H_4O_3$					
FEC (Fluoroethyl carbonate)	$C_3H_3FO_3$					
PC (Propylene carbonate)	$C_4H_6O_3$					
EMC (Ethyl methyl carbonate)	$C_4H_8O_3$					
FEMC (fluoroethyl methyl carbonate)	$C_4H_7FO_3$					
DEC (Diethyl carbonate)	$C_5H_{10}O_3$					
DMC (Dimethyl carbonate)	$C_3H_6O_3$					
VC (Vinylene Carbonate)	$C_3H_2O_3$					
Ma (Methyl acetate)	$C_3H_6O_2$					
Ea (Ethyl acetate)	$C_4H_8O_2$					

Table S1. Continued

	Molecular Formula	Structural Formular	Li^++molecule	HOMO	LUMO	Cell construction
Ep (Ethyl propionate)	$C_5H_{10}O_2$					
Eb (Ethyl butyrate)	$C_6H_{12}O_2$					
Mb (Methyl butyrate)	$C_5H_{10}O_2$					
Mp (Methyl propionate)	$C_4H_8O_2$					
Pb (Propyl butyrate)	$C_7H_{14}O_2$					
Bb (Butyl butyrate)	$C_8H_{16}O_2$					
Mf (methyl formate)	$C_2H_4O_2$					
An (acetonitrile)	C_2H_3N					
Pn (propionitrile)	C_3H_5N					
Bn (butyronitrile)	C_4H_7N					

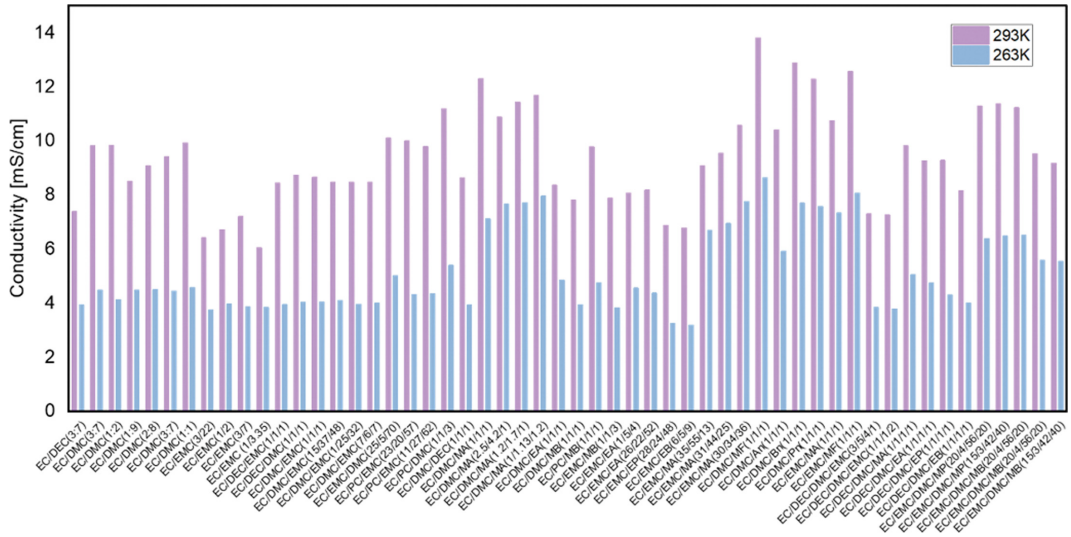


Fig. S2. Cell composed with Candidates. (a) EC/EMC, (b) EC/EMC/MA, (c) EC/EMC/MF cells consist of all substances in the same proportion.

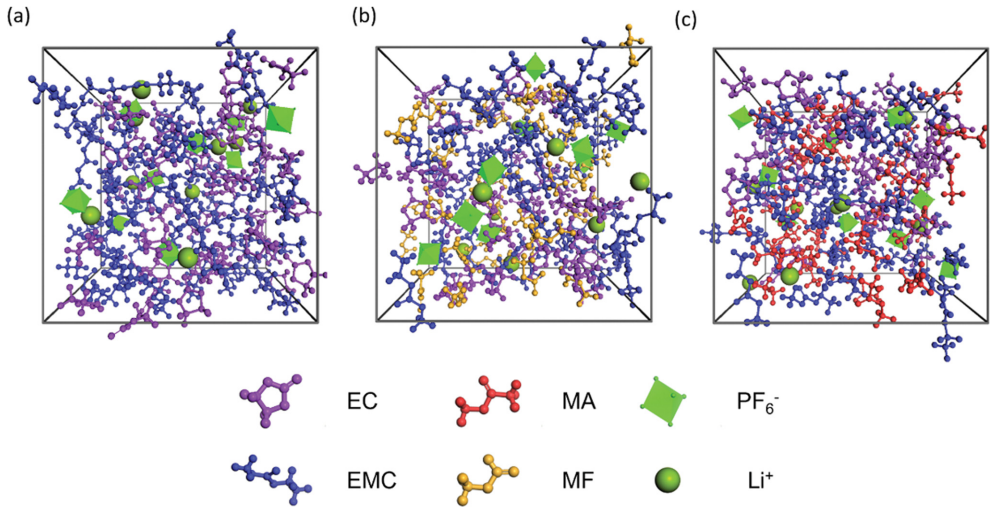


Fig. S3. Cell composed with Candidates. (a) EC/EMC, (b) EC/EMC/MA, (c) EC/EMC/MF cells consist of all substances in the same proportion.

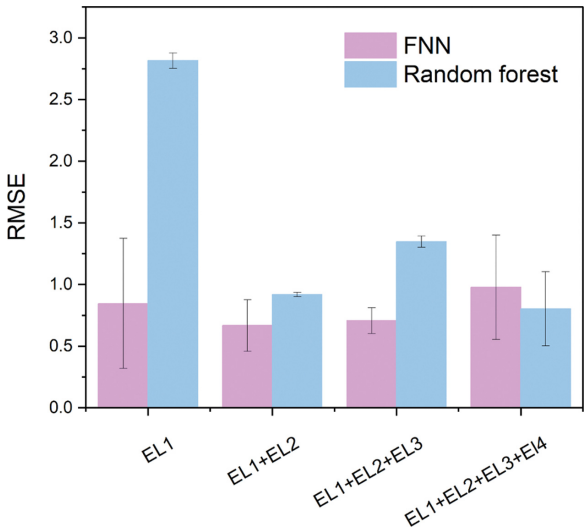
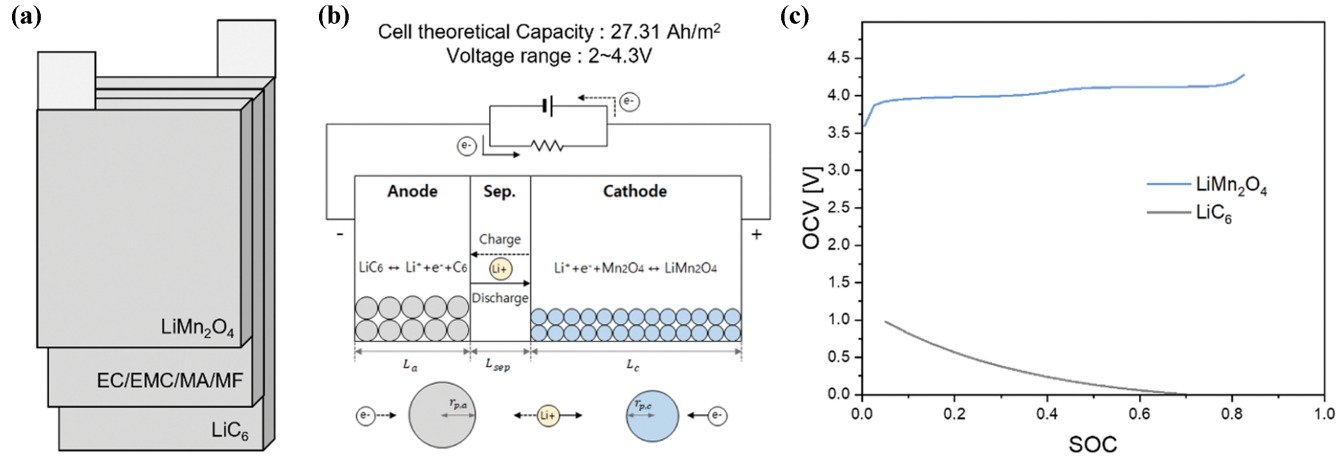


Fig. S4. Root mean square errors (RMSE) of FNN, Random Forest algorithm from single to quaternary solvents systems.



(d)

Parameters	Anode	Separator	Cathode
Thickness (μm) - L	100	52	183
Electrode volume fraction - r_p	0.471	-	0.297
Electrolyte volume fraction	0.503	-	0.63
Particle radius (μm)	12.5	-	8
Initial electrolyte concentration (mol/L)	-	2	-
Initial state of charge	0.56	-	0.17
Solid diffusivity (m^2/s)	3.9E-14	-	1E-13
Electric conductivity (S/m)	100	-	3.8
Maximum Li+ concentration (mol/m^3)	26,390		22,860
anodic charge transfer coefficient	0.5	-	0.5
cathodic charge transfer coefficient	0.5	-	0.5

Fig. S5. Information about full cell modelting. (a) Schematic of full cell modeling. (b) Cell geometry and cell theoretical capacity, (c) OCV curve of $LiMn_2O_4$ and Graphite [1], (d) Parameters table of details of cell system.

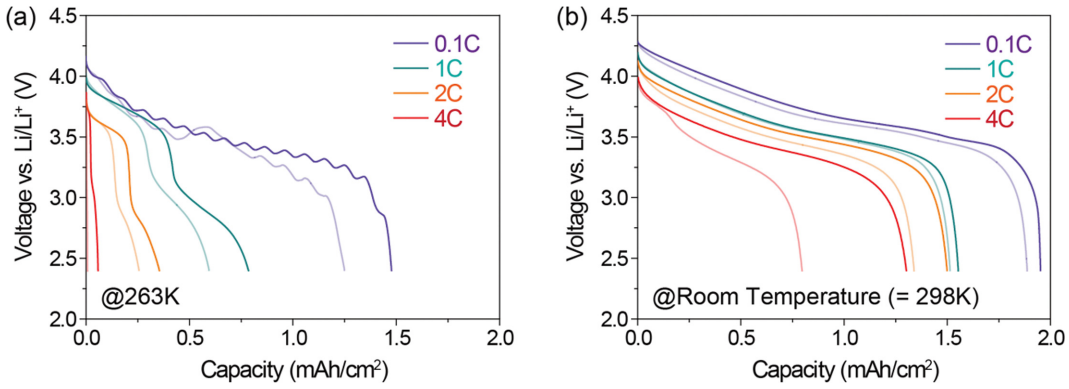


Fig. S6. Voltage profiles of NCM/Graphite full cells with different electrolytes at different C-rates and temperature of (a) 263 and (b) 298 K. Vivid and vague colors indicate the results of EC/EMC and EC/EMC/MA/MF electrolytes, respectively.

Experimental Section

Cell Assembly and Full-Cell Tests: To access the full-cell performance at 263 and 298 K, the cathode electrode was prepared by mixing $LiNi_{0.6}Co_{0.2}Mn_{0.2}O_2$ (NCM) powder with Super P (TIMCAL, Switzerland) and poly(vinylidene fluoride) (PVDF, Aldrich, USA) in a weight ratio of 94 : 3 : 3 in *N*-methyl-2-pyrrolidone (NMP, Aldrich, USA). Then, the homogeneously mixed slurry was cast on an Al foil (20 μm, Hohsen, Japan) using the doctor blade, followed by vacuum-drying at 80 °C for 12 h to remove any residual solvent. The final areal capacity of the NCM electrode was 2 mAh/cm^2. In addition, the graphite anode was prepared by mixing graphite, Super P, and PVDF in a weight ratio of 91 : 1 : 8, considering the N/P ratio of ~1.1. The EC/EMC/MA/MF electrolyte was prepared by dissolving 1 M lithium hexafluorophosphate ($LiPF_6$, Aldrich, USA) in

a cosolvent of ethylene carbonate (EC, Aldrich, USA)/ethyl methyl carbonate (EMC, Aldrich, USA)/methyl acetate (MA, Aldrich, USA)/ methyl formate (MF, Aldrich, USA) (1 : 1 :1 : 1=v : v : v : v). The control electrolyte was prepared by dissolving 1 M $LiPF_6$ in a cosolvent of EC/EMC (1 : 1=v : v). We assembled the coin-type cells (2032 type, Welcos, Korea) by incorporating the NCM cathode, polyethylene separator (PE, Celgard 2730, 20 μm), and a graphite anode. For a paired comparison, the same amount of electrolyte of 120 μL was added to the coin cell. The electrochemical tests were conducted in the voltage range of 2.4-4.3 V at different C-rates of 0.1, 1, 2, and 4 C. All of the electrochemical tests were performed using the coin-cells and a battery cycler (WBCS 3000, WonAtech, Korea) at 263 and 298 K.

REFERENCES

1. M. Doyle, J. Newman, A. S. Gozdz, C. N. Schmutz and J. M. Tarascon, *J. Electrochem. Soc.*, **143**, 1890 (1996).